Journal of Hazardous Materials Advances 10 (2023) 100321

Contents lists available at ScienceDirect

Journal of Hazardous Materials Advances

journal homepage: www.elsevier.com/locate/hazadv

Insight into the adsorption thermodynamics, kinetics, and photocatalytic studies of polyaniline/SnS_2 nanocomposite for dye removal

Nafees Ahmad[a,*], Daraksha Bano[a,b], Sabeeha Jabeen[a], Naseem Ahmad[a], Arshad Iqbal[c], Waris[d], Abdul Hakeem Anwer[e], Changyoon Jeong[e,*]

[a] Department of Chemistry, Integral University, Lucknow 226026, India
[b] Department of Chemistry, IIT BHU, Varanasi 221005, India
[c] Department of Physics, Integral University, Lucknow 226026, India
[d] Industrial Chemistry Research Laboratory, Department of Industrial Chemistry, Aligarh Muslim University, Aligarh 202002, India
[e] School of Mechanical Engineering, Yeungnam University, Gyeongsan, Gyeongbuk 38541, Republic of Korea

ARTICLE INFO

Keywords:
Nanocomposite
Thermodynamics
Kinetics
Photocatalytic
Adsorption
Heterojunction

ABSTRACT

The study aims to address the synthesis, the kinetics of adsorption, and photocatalytic application of Polyaniline/tin sulfide (PANI/SnS_2) nanocomposite against brilliant blue (BB) dye. PANI/SnS_2 was prepared by in-situ polymerization of the aniline to which hydrothermally synthesized SnS_2 was added. Adsorption thermodynamics and kinetics of PANI/SnS_2 were discussed against the BB dye using Langmuir and Freundlich adsorption isotherm. Maximum adsorption capacity (q_m) and adsorption equilibrium constant (K) were found to be 165.2 mg g^{-1}, and 0.027 min^{-1}. Moreover, Adsorption kinetics were studied by the pseudo-first and second-order reactions. The adsorption rate constant k_1 and diffusion rate constant k_2 were found to be 0.1274 and 0.0233 min^{-1}. PANI and SnS_2 with tunable band gap energy, adsorption, and redox property exhibited excellent activity towards the photodegradation of BB dye. The effect of heterojunction between PANI/SnS_2 was observed by an increased rate of transfer of electrons. The rate constant was highest in the case of PANI/SnS_2 (20%), which is 0.0172 min^{-1} and a maximum of 96.2% of BB dye was degraded in 45 min. The hydroxyl ($^{\bullet}OH$) and superoxide ($\bullet O_2^-$) radicals were generated during photocatalysis that degrades the BB dye into nontoxic products, which were confirmed by the trapping experiment. The obtained results indicate the excellent adsorption and photocatalytic activity of PANI/SnS_2 nanocomposite.

1. Introduction

Accumulation of toxic contaminants in the ecosystem has become one of the major concerns around the globe. The discharge of the toxic contaminants into the environment harms human beings, as well as aquatic species. With the rapid industrialization, the growth of these contaminants including pharmaceutical and personal care products (PPCPs), heavy metals, polyaromatic hydrocarbons (PAHs), fertilizers, ammonia, and textile dyes, is increasing day by day (Yontar et al., 2022; Bolisetty et al., 2019; Bag et al., 2022; Khan et al., 2023; Muslim et al., 2022). Among them, organic textile dyes which have been widely utilized in various industries are directly discharged into water streams, that results to high chemical oxygen demand (COD) after being treated by several methods (Guo et al., 2023; Lellis et al., 2019; Al-Tohamy et al., 2022; Ahmad et al., 2021). The toxic dyes if not degraded completely may result in the formation of hazardous products (Doh et al., 2008; Ghanbari and Moradi, 2017). Therefore, the removal of toxic dyes from water streams into nontoxic components is of considerable importance to resolving environmental concerns. For the last few decades, various physical, chemical, and biological methods are used to resolve the issues related to the treatment of wastewater (Bhatt et al., 2021; Varjani et al., 2020; Serrano-Martínez et al., 2020; Bhat and Gogate, 2021). However, certain drawbacks are associated with these methods made unreliable for practical implementation.

Now a day, in order to tackle the waste water problem, the advanced oxidation process is proven to be the most operational as it is quite efficient, less time-consuming, and doesn't involve the complex mechanism for the degradation of contaminants (Bhat and Gogate, 2021; Chen et al., 2022; Senasu et al., 2018). The basic necessity for the operation in advanced oxidation processes is the selection of photocatalysts. Photocatalysts with band gap energy that falls in the visible region are quite effective in the process. A number of semiconductor nanoparticles has already been used as photocatalysts for this purpose (Wu et al., 2015; Jenifer and Sriram, 2023; Benchikh et al., 2022; Sagadevan et al., 2022; Bano et al., 2020). However, the nanoparticles with high surface area enables them to be more reactive and

* Corresponding authors.
E-mail addresses: siddiquenafees123@gmail.com, anafees@iul.ac.in (N. Ahmad), yoonni22@yu.ac.kr (C. Jeong).

https://doi.org/10.1016/j.hazadv.2023.100321
Received 13 March 2023; Received in revised form 3 May 2023; Accepted 16 May 2023

highly activated upon illumination for the photocatalytic applications. Generally, a wide band gap semiconductor nanoparticles are used as heterogeneous photocatalysts and excellent redox ability of valence band (VB) and conduction band (CB). During the photocatalysis process, upon illumination with suitable energy equal to or more than the band gap energy (Eg) of the semiconductor, there is an excitation of electrons from the VB to the CB of the semiconductors. The photogenerated electrons and holes through redox reactions with H_2O, and atmospheric O_2 result in generation of $^{\bullet}OH$, and $^{\bullet}O_2^-$ radicals. These radicals degrade the contaminants present in the suspension into CO_2 and other minerals (Sagadevan et al., 2022). However, using single material based photocatalyst for the degradation of contaminants has a major drawback in the recombination of photogenerated charge carriers. Therefore, the formation of heterojunction for photocatalytic process is quite important as it reduces the recombine behavior of electrons and holes.

The combination of polymer and nanoparticle due to the synergistic effect has shown brilliant photocatalytic efficiency due to improved processability, surface area, stability, and tunable properties. Also, polymer nanocomposites (PNCs) find applications in other photocatalytic applications such as carbon dioxide reduction and water splitting and other biomedical applications (Bano et al., 2020). Tin sulfide (SnS_2) is a semiconductor nanoparticle with visible range band gap energy and excellent redox property used as photocatalysts for the removal of a wide range of recalcitrant organic contaminants (Akti and Balci, 2022; Zhang et al., 2022; Lei et al., 2009; Zhang et al., 2013; Gadore et al., 2023). Polyaniline (PANI) is widely used photocatalyst for the last few years due to its characteristic properties such as large surface area and redox ability along with relative high electrical conductivity (Akti, 2018; He et al., 2022; Toumi et al., 2022; Xu et al., 2018; Ahmad et al., 2022; Mahanta et al., 2011; Sayed et al., 2022). In the present study, PANI and semiconductor nanoparticles SnS_2 has been used to develop the heterojunction (PANI/SnS_2) by means of hydrothermal technique. The fabricated heterojunction shows excellent adsorption capacity and photocatalytic activity in the removal of BB dye. The rate of photodegradation of the BB-dye follows pseudo first order and pseudo second order along with high rate constant. Moreover, our designed heterojunction based photocatalyst is durable and can be used for practical purposes in the treatment of wastewater.

2. Experimental section

2.1. Materials and reagents

Analytical grade chemicals were used for all the experiments. Ammonium persulphate was purchased from Thermo Fisher Scientific India. Aniline LR was purchased from S.D. Fine-Chem. Ltd. Mumbai. Hydrochloric acid is also obtained from S.D. Fine-Chem. Ltd. Mumbai, while DMW used was prepared in the Chemical Laboratory. Stannic chloride, thioacetamide, and Brilliant Blue were purchased from Sigma Aldrich.

2.2. Synthesis of photocatalysts

2.2.1. Synthesis of polyaniline (PANI)

By using ammonium persulfate (APS) as an oxidant and aniline that had been dissolved in aqueous HCl (1 M), polyaniline was synthesized. Aniline (1 mmol) and APS (1 mmol) were dissolved in an aqueous solution of HCl (1 M). The aniline solution was then gradually mixed with the oxidant solution at a temperature of 25 °C and kept for the stirring for two hours. Further, the reaction mixture was filtered and washed it with HCl (0.5 M) until the filtrate was colorless, the filtrate was then washed with water until it was neutral. The resulting polymer was overnight dried at 60 °C in a vacuum oven (Ahmad et al., 2019).

2.2.2. Synthesis of tin sulfide (SnS_2) nanoparticles

To synthesize the SnS_2 nanoparticles, one-step hydrothermal procedure was used (Dashairya et al., 2019). In this procedure, stannic chloride ($SnCl_4{\cdot}5H_2O$) (1 mmol) and thioacetamide (TAA) (2 mmol) were mixed followed by 30 min of stirring. Further, the mixture was placed into a hydrothermal autoclave (Teflon-lined, 200 mL stainless steel) and kept at 180 °C for 24 h. The suspension was centrifuged and repeatedly rinsed with ethanol and distilled water after cooling to room temperature. The resultant dark yellow color precipitate was obtained and then dried for 12 h at 60 °C under a vacuum.

2.2.3. Synthesis of PANI/SnS_2 nanocomposite

By maintaining the varied weight fractions of SnS_2 to 10% and 20% to aniline during the in situ polymerization of aniline, PANI/SnS_2 nanocomposite was produced. An overview of the reaction scheme is presented in Fig.1.

An estimated quantity of aniline was dissolved in HCl solution (1 M). Then, this solution was sonicated for an hour while a calculated amount of synthetic SnS_2 was mixed in. The reaction mixture was then gradually supplemented with the APS solution while being vigorously stirred at room temperature for 4 h. The reaction mixture was then filtered, washed with distilled water to remove the impurities. The final nanocomposite was obtained after kept for drying at 60 °C in a vacuum oven.

2.3. Adsorption activity

The adsorption property of synthesized PANI/SnS_2 nanocomposite against BB dye was studied by the means of dynamic method (Chen et al., 2019). In this method, 100 mg of PANI/SnS_2 nanocomposite was first dispersed into 50 mL of an aqueous solution of BB dye solution followed by continuous stirring. To approach the adsorption equilibrium, the mixture was sealed and kept at room temperature. Further, the dye samples were taken out at a fixed intervals to check the concentration of BB dye. The concentration of BB dye was checked at 594 nm of wavelength. The amount of dye adsorbed on PANI/SnS_2 composite was calculated by the following Eq. (1):

$$\text{Amount of dye adsorbed} = \frac{C0 - Ce}{M} * V \quad (1)$$

Where, the initial dye concentration is denoted by C_0 and Ce is the dye concentration at the equilibrium condition, volume of the dye solution is denoted by V (L) and the mass of PANI/SnS_2 is denoted by M (g) that were taken. Adsorption thermodynamics using Langmuir and Freundlich adsorption isotherm and adsorption kinetics using pseudo-first-order (adsorption) and pseudo-second-order (diffusion) were studied by the results obtained. Moreover, the percentage adsorption efficiency (AE) of PANI/SnS_2 against BB dye was calculated by following Eq. (2)

$$\text{Adsorption efficiency}\,(\%) = \frac{C0 - Ct}{C0} * 100\% \quad (2)$$

2.4. Photocatalysis, trapping and recycling studies

The photocatalytic activity of PANI, SnS_2, and PANI/SnS_2 (10% and 20%) investigated towards the degradation of BB dye. The photodegradation process starts with the adsorption step. In a typical procedure, 100 mg of PANI, SnS_2, and PANI/SnS_2 (10% and 20%) dispersed into 100 mL of an aqueous solution of dye under continuous stirring. The mixture was kept with continuous stirring without light for 45 min to reach the adsorption–diffusion equilibrium between photocatalyst and the BB dye. Further, a visible lamp (power 500 W) used to illuminate the suspension under constant stirring. At regular intervals of time, 5 mL of aliquots were taken out and centrifuged. Then the concentration of aliquots was recorded by spectrophotometer at wavelength 555 nm. The

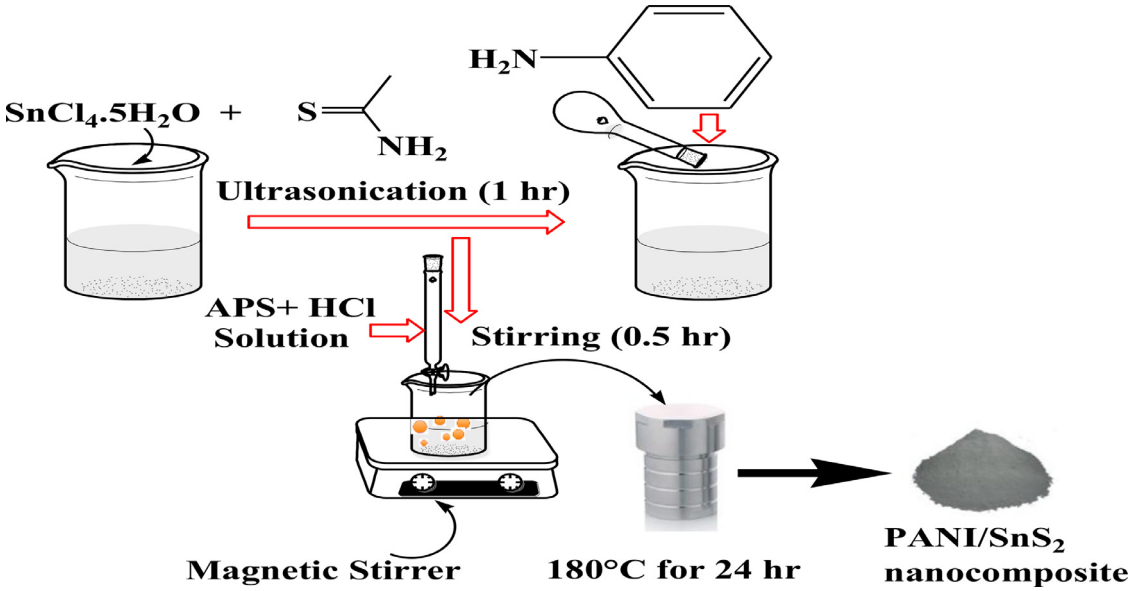

Fig. 1. Overview of the reaction for the synthesis of PANI/SnS_2 nanocomposite.

obtained data were used to study the kinetics and rate constant calculation of photocatalysts. The amount of BB dye degraded by PANI, SnS_2, and PANI/SnS_2 (10% and 20%) by using the following Eq. (3)

$$\text{Amount of dye adsorbed} = \frac{Ce - Ct}{M} * V \tag{3}$$

where Ce and Ct are the concentration of BB dye at adsorption equilibrium and at a time 't' respectively, V (L) and M (g) are the volume of dye solution, and mass of the photocatalysts respectively. Further, the percentage degradation efficiency of the photocatalysts against the BB dye was calculated by following Eq. (4).

$$\text{Degradation efficiency}\,(\%) = \frac{Ce - Ct}{Ce} * 100\% \tag{4}$$

Additionally, to ensure the main reactive oxygen species accountable for the degradation of the BB dye, trapping agents were added during photocatalysis to quench the reactive species. In the procedure, t-butyl alcohol (TBA), ethylenediaminetetraacetic acid (EDTA) and p-benzoquinone was used to quench $^{\bullet}OH$, h^+ and $^{\bullet}O_2^-$ respectively. Moreover, to confirm the durability of the prepared sample, the experiment of photodegradation for BB dye was repeated successively without changing the sample (photocatalyst).

2.5. Materials characterization

The synthesized materials were analyzed by various characterization equipment. Transmission electron microscopy (TEM, TECHNAI G^2 20 S TWIN) was used to ensure the formation of nano-range composites. The X-ray diffractometer (BRUKER D8 ADVANCE 30 kV and 15 mA) was used to analyze crystallite size and geometry of the materials. FTIR (Fourier transform infrared spectroscopy-Perkin Elmer spectrum-2, USA) was probed to analyze the functional groups in the range of 400–4000 cm^{-1}. SEM-EDX (JSM 6510 LV JEOL Japan) was used to examine the surface morphology and elemental composition. The absorbance of the degraded BB dye samples were checked using ultraviolet-visible spectroscopy (Thermo scientific Evolution 201-USA), and fluorescence spectroscopy (Hitachi-F-2500-Japan) was used to check the photoluminescence intensity of charge carriers. Using Brunauer-Emmett-Teller, the surface area, pore size, and volumes were estimated (Quantachrome Instruments version 5.21).

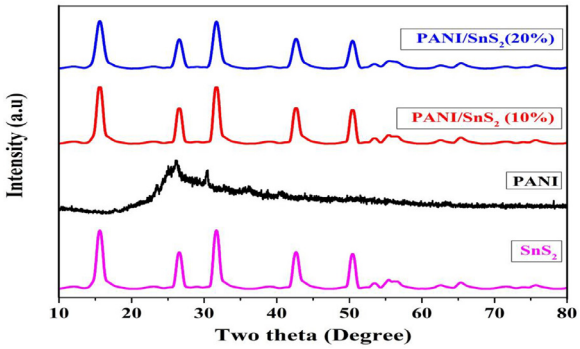

Fig. 2. XRD spectra of the PANI, SnS_2 and PANI/ SnS_2 nanocomposite.

3. Results and discussion

3.1. The analysis of X-ray diffraction

X-ray diffraction (XRD) was utilized for the estimation of crystallite size and the nature of the photocatalysts. The XRD spectra of PANI, SnS_2, and PANI/SnS_2 with 10% and 20% composition are presented in Fig. 2.

The intense peaks of SnS_2 exhibit the crystalline nature whereas the broad hump in the case of PANI shows the amorphous nature. There is no shift occurring upon doping of SnS_2 to the PANI indicating that no angle of strain was observed in the PANI/SnS_2 nanocomposite. The peaks at angle two theta of the PANI are 25.4° and the corresponding hkl values are 200 (Xiong et al., 2013) and the peaks at the angle at 31.9°, 41.2°, 58.3°, 68.7°, 75.4° with corresponding hkl value 101, 102, 110, 111, 201 indicates the crystalline nature of SnS_2 nanoparticles and PANI/SnS_2 nanocomposite (Wu et al., 2015; Zai et al., 2021) The crystallite size of PANI, SnS_2 and PANI/SnS_2 with 10% and 20% were calculated by Sherrer's formula as given below (Sultana et al., 2017).

$$D = \frac{0.9\lambda}{\beta cos\theta} \tag{5}$$

Where the average crystallite size is denoted by d, the wavelength of X-ray is represented by λ, full width at half maxima is denoted by β, and Bragg's angle is represented by θ for the diffraction peaks in 2θ starting from 10° to 80° The estimated crystallite size of SnS_2, and PANI/SnS_2

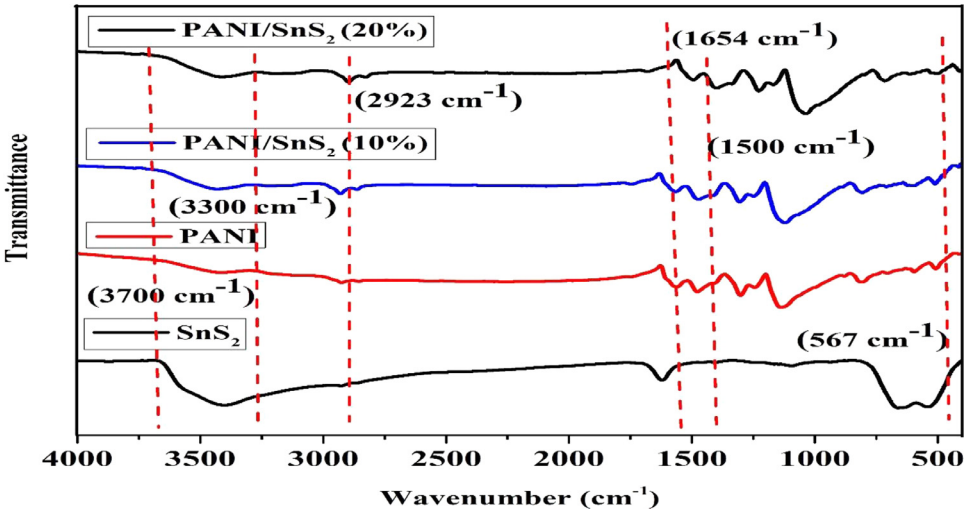

Fig. 3. FTIR spectra of the as prepared PANI, SnS_2 and PANI/SnS_2 nanocomposite.

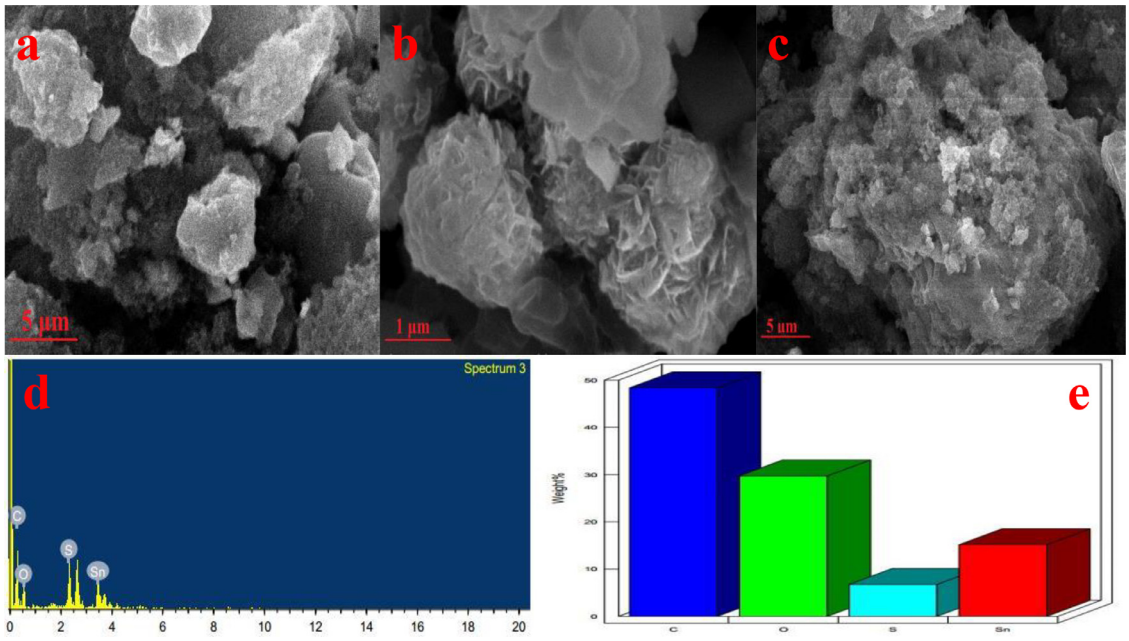

Fig. 4. SEM image of (a and b) SnS_2 and (c) PANI/SnS_2 and EDX image of PANI/SnS_2 (d,e).

with 10% and 20% were found to be 31.7 nm, 43 nm, and 67.4 nm respectively.

3.2. Functional group analysis (FTIR)

For the analysis of the functional group present in PANI, SnS_2, and PANI/SnS_2 -nanocomposites FTIR technique was used. FTIR spectra of PANI, SnS_2, and PANI/SnS_2 are presented in Fig. 3.

The spectrum of PANI clearly shows the absorption peaks at 1654 and 1637 cm^{-1} are due to stretching in aromatic nuclei. The polymer shows absorption bands in the region 2923–2800 cm^{-1} due to asymmetric C–H stretching vibrations (Khan et al., 2014). The peaks at 3300–3700 cm^{-1} were attributed to N–H stretching and the bands at 1600–1500 cm^{-1} correspond to C–H stretching in aromatic compounds. The peaks that appeared at 567 cm^{-1} are due to Sn-S Stretching vibration (Yang et al., 2013; Saadati and Sheibani, 2022) which shows the formation of PANI/SnS_2 nanocomposite.

3.3. Thermal analysis

Thermal analysis of PANI, SnS_2, and PANI/SnS_2 NCs have been performed to check the stability under nitrogen atmosphere by using thermogravimetric analysis (TGA) and differential thermal analysis (DTA) in the temperature range of 0–800 °C shown in Fig. S1. Weight loss analysis of the prepared nanocomposites PANI observed in three region, the first region is up to 200 °C which is due to which is due to evaporation of the physical water adsorbed on the surface of the nanocomposites and second region is between 200 to 400 °C at the midpoint of 321.68 and the weight loss of −3.711 mg which is due to loss of solvents is the synthesis of the nanocomposites and the region is between 400–750 °C due to removal of the lattice water and thermo-oxidative decomposition of PANI (Lin et al., 2017; Nepomuceno et al., 2021). The weight loss of the nanocomposites (PANI/SnS_2) observed at the mid-point (109.2, 320.30, 622.81) is −0.135 −0.805, and −2.102 mg respectively. Among the three samples, tin chloride is the most stable over the entire range of temperatures however PANI is the least stable. Upon doping of SnS_2 to the PANI the stability of the PANI/SnS_2 has been improved, as shown in the Fig. S1.

3.4. Microscopic studies

A scanning electron microscope coupled with energy dispersive x-ray spectroscopy (SEM-EDX) was used to study the surface morphology and elemental composition of the PANI/SnS_2 nanocomposite. The SEM

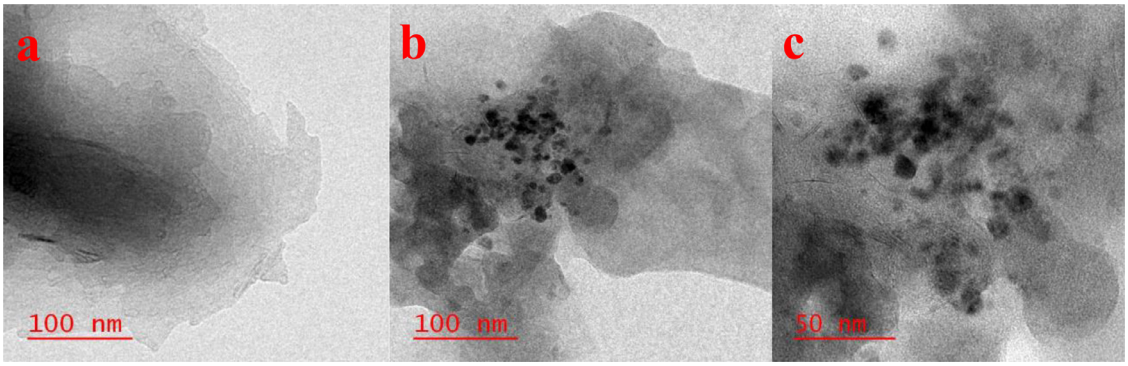

Fig. 5. TEM image of (a) PANI and (b, c) PANI/SnS_2 nanocomposites at different magnifications.

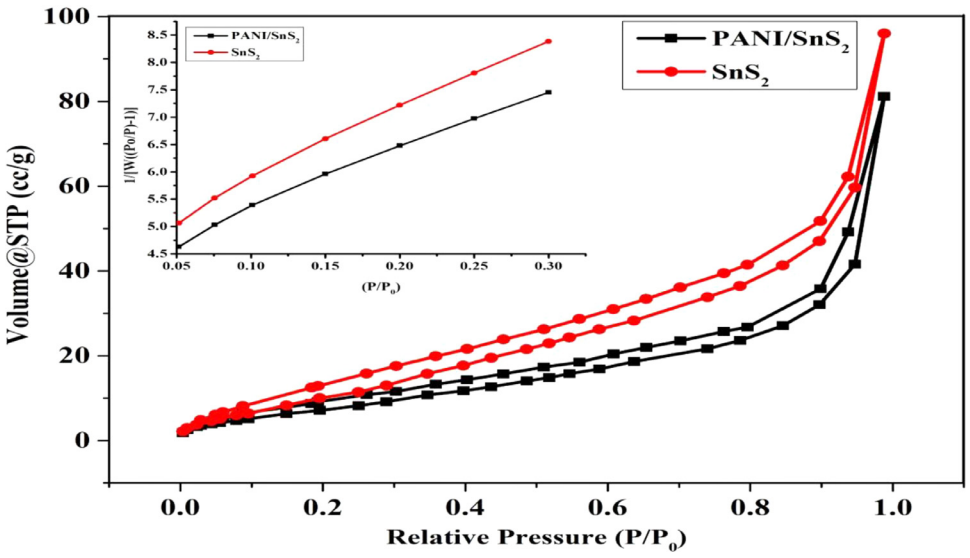

Fig. 6. BET image of SnS_2 and PANI/SnS_2 (20%).

image of SnS_2 nanoparticles are presented in 4 (a, b) and PANI/SnS_2 is presented in Fig. 4(c). From the figure spherical shape of SnS_2 nanoparticles can be clearly seen. And in the composite the particle of the SnS_2 are agglomerated over the porous surface of the PANI. The surface morphology of the PANI has been changed by the incorporation of the SnS_2 as the pores of the PANI are covered which also reduces the surface area of the PANI/SnS_2 nanocomposites (Matyszczak et al., 2021).

The elemental analysis of the PANI/SnS_2 nanocomposites were probed by the EDX analysis, which confirms that carbon (C), oxygen (O), sulfur (S), and tin (Sn) were the major elements in the synthesized matrix, as shown in Fig. 4(d, e).

Further, the TEM micrographs of PANI and PANI in the presence of SnS_2 confirms the formation of PANI/SnS_2 composites in nano-range, as shown in Fig. 5(a, b). The high-resolution TEM image of PANI/SnS_2 nanocomposite is given in Fig. 5c whereas TEM image of SnS_2 nanoparticles is provided in Fig. S2. Moreover, the formation of composite in nano-range and the size of the particles can be confirmed with the results obtained from XRD analysis.

3.5. BET analysis for the surface area

Brunauer–Emmett–Teller (BET) method was used to determine the specific surface areas, and pore volumes of SnS_2 and PANI/SnS_2 (20%) using nitrogen adsorption-desorption isotherm. The surface area and pore radius of SnS_2 are 23.271 m^2/g, and 28.73 Å respectively, and the surface area and pore radius of 20% PANI/SnS_2 are 27.532 m^2/g and 19.13 Å respectively, as presented in Fig. 6.

The higher surface area of PANI/SnS_2 (20%) as compared to pure SnS_2 is due to the formation of composites of PANI/SnS_2 (Parveen et al., 2016; Nawaz et al., 2022). The adsorption-desorption isotherm of SnS_2 and PANI/SnS_2 shows hysteresis loop clearly indicates the formation of mesoporous composites. The higher surface area of PANI/SnS_2 (20%) is the reason for showing higher photocatalytic activity and adsorption of dye than pure SnS_2.

3.6. Bandgap energy and edge band potential analysis

The band gap energy of SnS_2, PANI/SnS_2 (10%), and PANI/SnS_2 (20%) were calculated by Tauc's relationship between absorbance coefficient (α) and bandgap (Eg) as shown below,

$$(\alpha h\nu)^n = A(h\nu - E_g) \quad (6)$$

where α, hν and E_g denotes the absorption coefficient, energy of the photon and the bandgap energy respectively. The plot of $(\alpha h\nu)^2$ Vs E_g is shown in Fig. S3 to determine the band gap energy of SnS_2, PANI/SnS_2 (10%), and PANI/SnS_2 (20%). The tangent line drawn to the x-axis indicate the bandgap energies of the photocatalysts. The estimated band gap energies for SnS_2, PANI/SnS_2 (10%), and PANI/SnS_2 (20%) were found to be 2.45, 2.3 and 2.24 eV, respectively which is in the range of values of reported literature (Zhang et al., 2014).

3.7. Evaluation of adsorption thermodynamics

The adsorption thermodynamics were investigated by varying the initial concentration of BB dye ranges from 10 to 190 ppm with photocatalyst, as shown in Fig. 7. The adsorption performances of PANI,

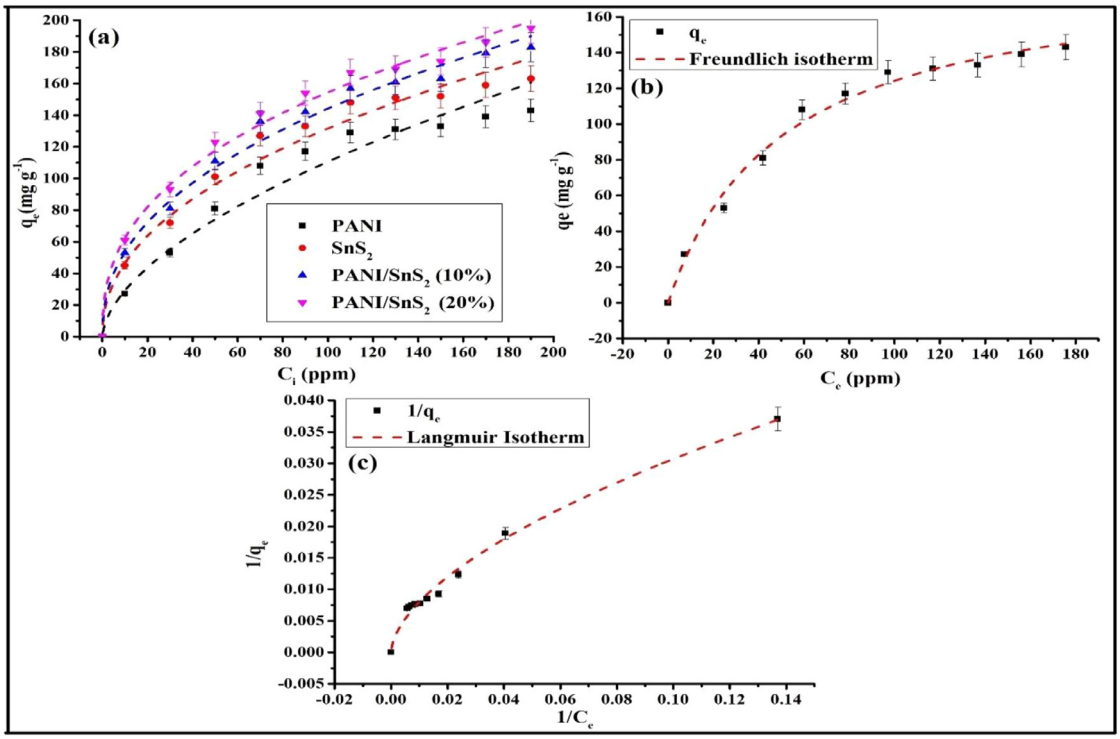

Fig. 7. (a) Adsorption capacity of the BB-dye (b) plot of Freundlich adsorption isotherm and (c) Langmuir adsorption isotherm.

Table 1
Comparison of Langmuir and Freundlich isotherm on the adsorption capacity of photocatalysts.

Langmuir isotherm		
Maximum Adsorption capacity q_m (mg g^{-1})	Adsorption constant (K_L)	Correlation coefficient R_L^2
165.2	0.027	0.9794
Freundlich isotherm		
Adsorption constant (K_F)	Adsorption intensity (n)	Correlation coefficient R_F^2
2.27	1.66	0.990

SnS_2, and PANI/SnS_2 were investigated with the help of Langmuir and Freundlich isotherm adsorption models, by the following equation:

$$\mathrm{Log}q_e = \log K_f + \frac{1}{n}\log C_e \tag{7}$$

$$\frac{Ce}{qe} = \frac{Ce}{qe} + \frac{1}{KL\ qm} \tag{8}$$

Where K_f and K_L are Freundlich's equilibrium constant and Langmuir adsorption and n is a constant associated to the Freundlich adsorption intensity, qe is the equilibrium adsorption capacity of photocatalysts and qm is the maximum adsorption capacity of photocatalysts (Ayub et al., 2020; Abdullah and Chong, 2010). The Langmuir and Freundlich adsorption isotherms of BB-dye are shown in Fig. 7.

The fitting parameters and correlation coefficients of Langmuir model and Freundlich model are summarized and listed in Table 1.

The adsorption of BB dye on PANI/SnS_2 is determined to correspond to monolayer adsorption rather than multilayer adsorption, with the Langmuir model providing improved fitting to the equilibrium data than the Freundlich model with a higher correlation coefficient of 0.93 than 0.90.

3.8. Assessment of adsorption kinetics

The choice of the ideal operating environment for practical systems depends on the kinetics of dye removal. Then, two kinetic models were utilized to assess the investigational data and determine the finest fitting for the adsorption of dye by the photocatalyst to investigate the governing mechanisms of the adsorption method, for example transfer and chemical reaction. According to the first diffusion process, a concentration gradient between the bulk and interface drives the diffusion of numerous dye molecules to the surface of adsorbent. The initial diffusion process has a relationship between the concentration of dye and photocatalyst adsorption sites for the diffusion kinetic rate. As a result, the diffusion process is examined using the kinetic model of pseudo-second order in order to choose the model that best fits the experimental data.

$$\frac{d\theta t}{dt} = k_d^2(\theta e - \theta t) \tag{9}$$

$$\ln(\theta e - \theta t) = \ln\theta e - K_a t \tag{10}$$

Where the coverage fractions adsorbed at time t and equilibrium, respectively, are represented by t and e. For the diffusion process, kd is the pseudo-second-order reaction rate constant, while for the adsorption process, ka is the pseudo-first-order reaction rate constant. A pseudo-second-order rate expression is used to express the adsorption rate constant and is given as:

$$\ln(q_e - q_t) = \ln q_e - K_1 t \tag{11}$$

$$\frac{t}{qe} = \frac{1}{K_2\ qe^2} + \frac{1}{qe} \tag{12}$$

Where q_e and q_t (mg g^{-1}) are the amount of dye adsorbed at equilibrium and at time t, the adsorption time is denoted by t (min), and the rate constant of pseudo-first-order and pseudo-second-order reaction are

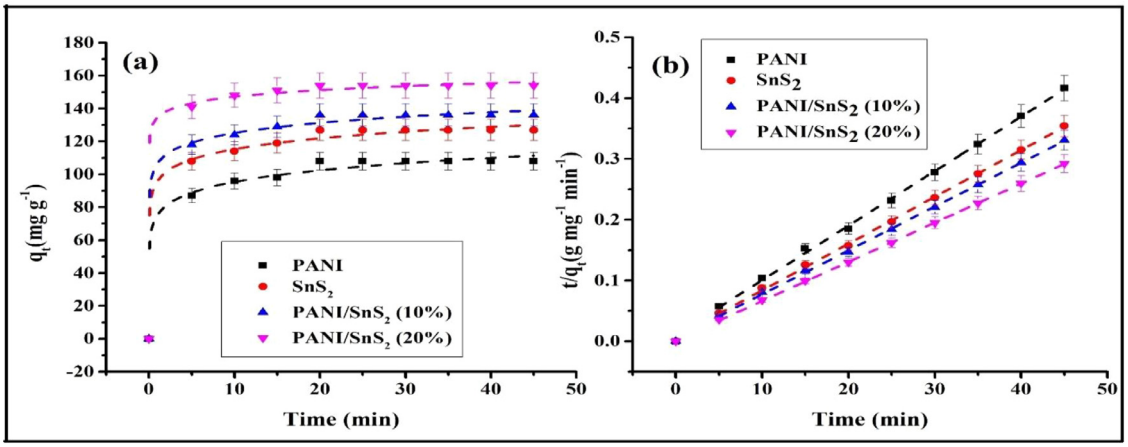

Fig. 8. (a) Kinetics of pseudo first order and (b) pseudo second order for SnS_2, PANI, PANI/SnS_2 (10%) and PANI/SnS_2 (20%).

Table 2
Comparison of pseudo first order and pseudo second order kinetics parameter of various catalysts.

Pseudo second order reaction (diffusion)				
Photocatalysts	Fitting equation $\frac{t}{qe} = \frac{1}{K_2\, qe^2} + \frac{1}{qe}$	Rate constant (K_2) (g mg^{-1} min^{-1})	Correlation coefficient R_d^2	Standard Deviation
PANI	$\frac{t}{qe}$ = 0.009t + 0.0086	0.0094	0.9987	0.12995
SnS_2	$\frac{t}{qe}$ = 0.0372t + 0.0597	0.0184	0.9945	0.11108
PANI/SnS_2 (10%)	$\frac{t}{qe}$ = 0.0348t + 0.0564	0.0215	0.9944	0.10401
PANI/SnS_2 (20%)	$\frac{t}{qe}$ = 0.0308t + 0.0516	0.0233	0.9939	0.09256
Pseudo first order reaction (adsorption)				
Photocatalysts	Fitting equation ln (qe-qt) = lnqe- K_1t	Rate constant (K_1) (g mg^{-1} min^{-1})	Correlation coefficient R_a^2	Standard Deviation
PANI	=3.607-(−0.1474)t	0.1474	0.750	1.586
SnS_2	=3.597-(−0.1363)t	0.1363	0.752	1.862
PANI/SnS_2 (10%)	=3.563-(−0.1357)t	0.1357	0.748	2.001
PANI/SnS_2 (20%)	=3.211-(−0.1274)t	0.1274	0.723	2.282

denoted by k_1 and k_2 (g $mg^{-1}min^{-1}$) for the diffusion process. The kinetic investigational data studied with the help of pseudo-first-order and pseudo-second-order models are represented in Fig. 8(a) and (b).

The equations of fitting and kinetic parameters for the dye adsorption which is calculated with the help of the pseudo-first-order and pseudo-second-order kinetic models plots are shown in Table 2.

The values of high correlation coefficient for photocatalysts (R_d^2 = 0.9987 and R_a^2 = 0.750) were obtained to be around 1, indicating that the adsorption kinetics of photocatalysts followed both the pseudo-first and second-order equations. Therefore the rate of the process can be controlled by diffusion as well as adsorption processes.

3.9. Assessing of photocatalytic activity and kinetics of photodegradation

The photocatalytic mechanism starts with the irradiation of visible light as a source of energy. A probable mechanism of the photodegradation of dye is presented in Fig. 9.

The irradiation of visible light results in the generation of electron-hole pairs in the photocatalyst from the valence band (VB) and conduction band (CB). The electron from the VB of SnS_2 and PANI excite and drift to their respective CB. Now to minimize the recombination of photogenerated pairs of electron and hole. The photogenerated holes in the VB of PANI and photogenerated electron in CB of SnS_2 will recombine because of almost similar edge band potential. Now the electron in the CB of PANI will react with atmospheric O_2 to create $^{\bullet}O_2^-$ radicals. Since the photogenerated holes in the VB of SnS_2 do have not sufficient potential (E^0 =2.27 eV vs NHE) to oxidize H_2O so $^{\bullet}O_2^-$ will react with H_2O to form H_2O_2 and $^{\bullet}$OH radicals. Now the photogenerated holes in the VB of SnS_2 which has the potential to oxidize the H_2O_2 molecule thereby generating hydroxyl radical ($^{\bullet}$OH) (E^0=0.80 eV vs NHE). Formation of reactive species i.e. e-, $^{\bullet}$OH, h^+, $^{\bullet}O_2^-$ due to the breaking of water molecules results in the degradation of the BB-dye (Ahmad et al., 2019; Iqbal et al., 2021; Rahman et al., 2020; Rahman et al., 2020; Sultana et al., 2020). In the case of PANI and SnS_2 when used as a bare photocatalyst, the degradation rate is very low. However, upon the doping of SnS_2 to PANI the photocatalytic activity enhanced which is due to the suppression of the recombination of photogenerated electrons and holes. The following general reaction is the degradation of the dye is given below:

$$PANI/SnS_2 + h\upsilon \rightarrow (e^- + h^+) \quad (13)$$

$$PANI(e-)O_2 \rightarrow \cdot O_2^- \quad (14)$$

$$\cdot O_2^- + H_2O \rightarrow \cdot OOH + {}^-OH \quad (15)$$

$$\cdot OOH + H_2O \rightarrow H_2O_2 + \cdot OH \quad (16)$$

$$SnS_2(h^+) + H_2O_2 \rightarrow \cdot OH \quad (17)$$

$$O_2-/\cdot OH/h^+ + BBDye \rightarrow CO_2 + H_2O \quad (18)$$

The UV–visible spectra of photo degraded samples of BB dye against PANI, SnS_2 and PANI/SnS_2 (20%) are shown in Fig. 10(a)–(c). After the optimization process of the reactor, the kinetics of the photodegradation of the BB-dye was investigated which shows the highest photodegradation rate in PANI/SnS_2 (20%). The kinetics of dye degradation by the photocatalysts are shown in Fig. 10(d).

Further, to estimate the rate constant, the residual concentrations of the dye were plotted as In C/C_0 vs. irradiation time, a plot of (C/C_0)

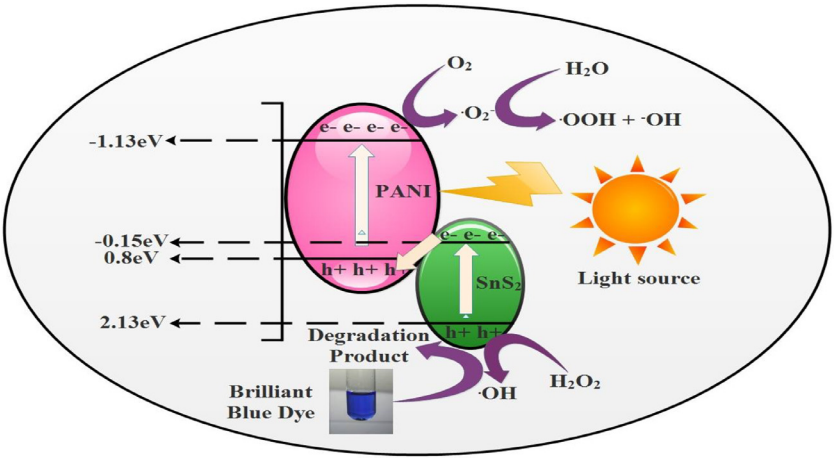

Fig. 9. Probable mechanism for the photodegradation of the brilliant blue dye.

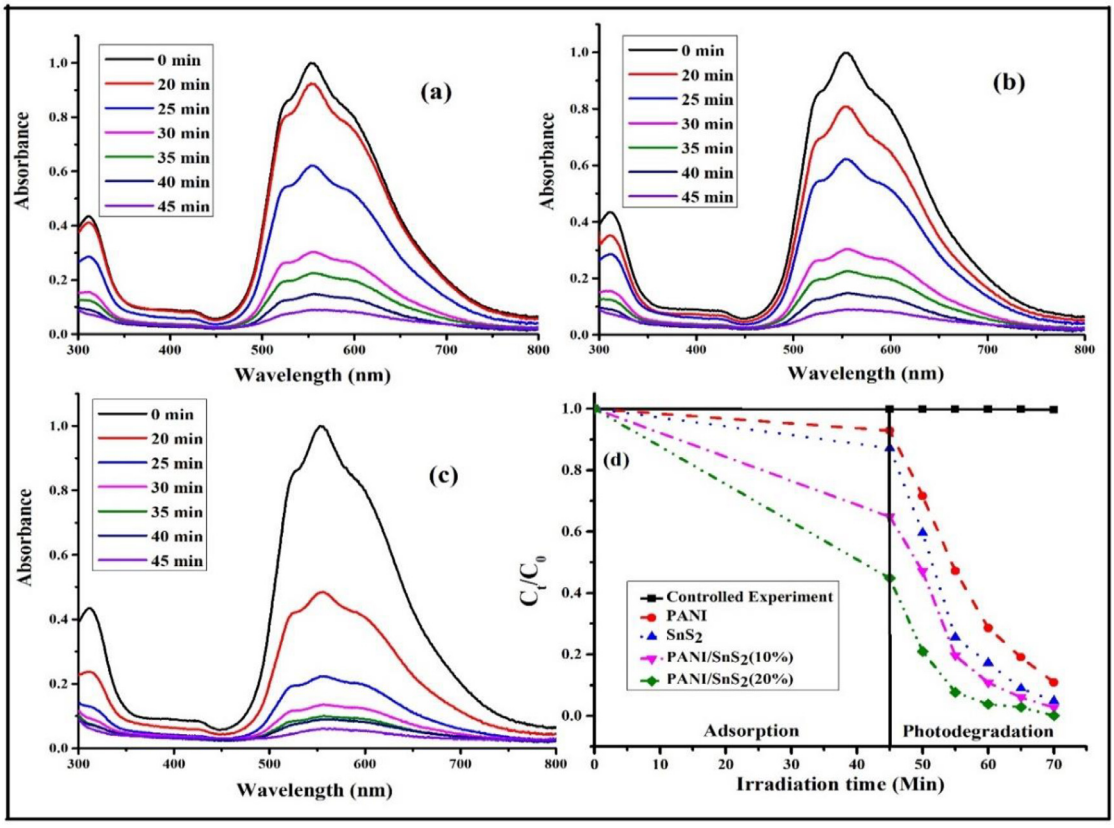

Fig. 10. UV–Visible spectra of the as degraded sample of BB dye against (a) PANI, (b) SnS_2 and (c) PANI/SnS_2 (20%) (d) plot of kinetics of photodegradation.

against irradiation time gives a straight line as shown in Fig. 11 which shows the first order kinetics are followed:

$$\frac{C}{C_0} = e^{-kt} \tag{19}$$

$$ln\left[\frac{C}{C_0}\right] = -kt \tag{20}$$

Where the initial concentration is represented by C_0 and the dye concentration at time'‘t’ is denoted by C. The rates constant calculated from the above formula are 0.00017, 0.01282, 0.03571, 0.04571 and 0.07983 min^{-1} for controlled experiment, PANI, SnS_2, PANI/SnS_2 (10%), and PANI/SnS_2 (20%) respectively. The degradation efficiency was found to be highest in the case of PANI/SnS_2 (20%) is 96.2%.

The fluorescence spectroscopy was used to determine the recombination rate of photogenerated electron-hole pairs which measures the photoluminescence (PL) intensity that depends upon the recombination rate of electron-holes pairs. The fluorescence spectra of PANI, SnS_2, and PANI/SnS_2 (10% and 20%) are presented in Fig. S4. The higher recombination rate of the electron and hole is directly proportional to the PL intensity. It is clear from the PL spectra that the lower recombination was observed in the case of PANI/SnS_2 (20%) photocatalyst, which has the highest photocatalytic activity.

3.8. Durability and trapping experiment

To confirm the durability of the photocatalysts, a recycling experiment was performed. For this process, the photocatalyst PANI/SnS_2 (20%) was recovered, centrifuged, and washed with DW and acetone

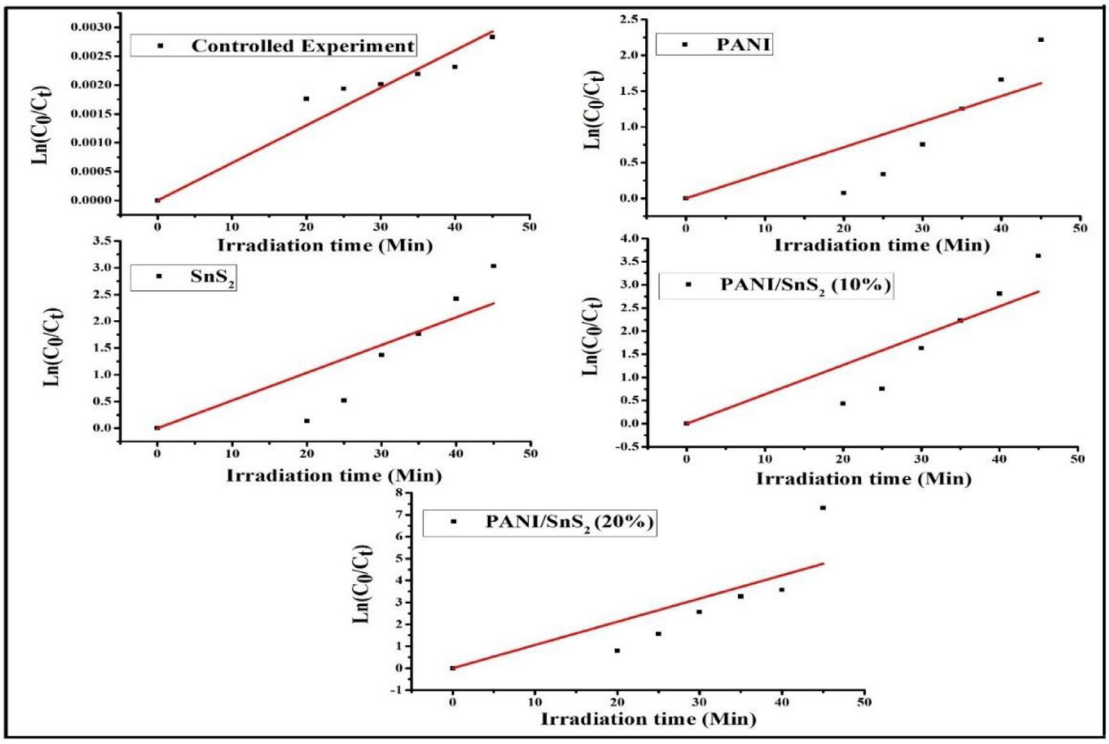

Fig. 11. Rate constant curve of controlled experiment, PANI, SnS_2 and PANI/SnS_2 (10% and 20%).

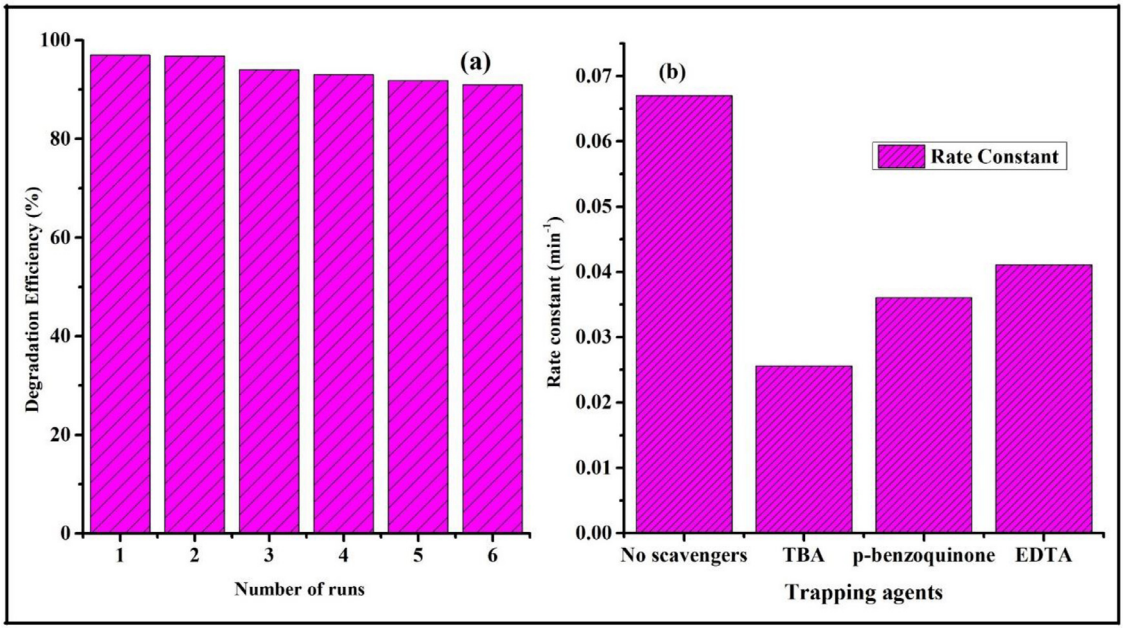

Fig. 12. (a) Recycling experiment of PANI/SnS_2 (20%, b) trapping experiment using various scavengers.

to remove the impurities and again used for six consecutive cycles. After the six cycles, there is only a slight decrease (4.7%) in the degradation efficiency of PANI/SnS_2 (20%) which shows the stability of the photocatalyst as shown in Fig. 12(a). Further, to ensure the effect of scavengers, 2 mM of each EDTA, TBA, and p-benzoquinone to quench h^+, ·OH and $\cdot O_2^-$, respectively were added in photocatalytic reaction (Ahmad et al., 2017; Khan et al., 2020) and simultaneously observed the rate of photodegradation. The rate constant is larger when no scavengers were added, as seen in Fig. 12(b), but when EDTA, TBA, and p-benzoquinone were added one by one, there is a considerable decrease in the rate constant. The lowest photodegradation was observed in the case of TBA suggesting that ·OH radicals are the primary reactive species causing a major effect in the photocatalytic activity. However, all the reactive species i.e. h^+, ·OH and $\cdot O_2^-$ are responsible for the degradation of BB dye.

Moreover to confirm the stability of the photocatalyst XRD was performed after the use of PANI/SnS_2 (20%) and no change in the peak shift was observed as shown in Fig. S5. It can be concluded that the photocatalyst is durable and can be used for practical purposes in the treatment of wastewater.

4. Conclusions

To conclude, the SnS_2 doped PANI photocatalyst has shown excellent adsorption and photocatalytic activity towards BB dye. The photocatalytic activity of PANI is increased by 37% upon doping of SnS_2 nanoparticles which is attributed to the recombination of photogenerated electrons and holes and the generation of more reactive oxygen species. Using a photocatalyst of the binary compound, the rate of transfer of electrons has been increased resulting in the formation of more reactive species. The photocatalyst followed Langmuir and Freundlich adsorption isotherm and the maximum adsorption capacity is found to be 165.2 (mg g^{-1}) and maximum photocatalytic activity is found to be 96.2% in the case of PANI/SnS_2 (20%). The correlation coefficient value (R^2 = 0.997 and 0.750), which shows the rate followed by pseudo first and second-order kinetics. Owing to excellent adsorption capacity, surface area, and photocatalytic activity, PANI/SnS_2 (20%) has shown a dual role in the removal of BB dye. With the results obtained, it can be concluded that the photocatalyst can be used for practical implementation in industries for the treatment of wastewater.

Funding information

The corresponding authors declare that no funding sources are available for this research work.

Declaration of Competing Interest

The authors declare that they have no known competing financial interests or personal relationships that could have appeared to influence the work reported in this paper.

Data availability

The data that has been used is confidential.

Acknowledgments

Authors are thankful to Department of Chemistry, Integral University, for providing necessary research facilities. Authors are also thankful to the R & D cell of the University for providing the Manuscript Communication Number (IU/R&D/2023-MCN0001837).

Supplementary materials

Supplementary material associated with this article can be found, in the online version, at doi:10.1016/j.hazadv.2023.100321.

References

Abdullah, M.A., Chong, F.K., 2010. Dual-effects of adsorption and photodegradation of methylene blue by tungsten-loaded titanium dioxide. Chem. Eng. J. 158 (3), 418–425.
Ahmad, N., Sultana, S., Azam, A., Sabir, S., Khan, M.Z., 2017. Novel bio-nanocomposite materials for enhanced biodegradability and photocatalytic activity. New J. Chem. 41 (18), 10198–10207.
Ahmad, N., Sultana, S., Kumar, G., Zuhaib, M., Sabir, S., Khan, M.Z., 2019a. Polyaniline based hybrid bionanocomposites with enhanced visible light photocatalytic activity and antifungal activity. J. Environ. Chem. Eng. 7 (1), 102804.
Ahmad, N., Sultana, S., Faisal, S.M., Ahmed, A., Sabir, S., Khan, M.Z., 2019b. Zinc oxide-decorated polypyrrole/chitosan bionanocomposites with enhanced photocatalytic, antibacterial and anticancer performance. RSC Adv. 9 (70), 41135–41150.
Ahmad, N., Anae, J., Khan, M.Z., Sabir, S., Yang, X.J., Thakur, V.K., Coulon, F., 2021. Visible light-conducting polymer nanocomposites as efficient photocatalysts for the treatment of organic pollutants in wastewater. J. Environ. Manag. 295, 113362.
Ahmad, N., Anae, J., Khan, M.Z., Sabir, S., Campo, P., Coulon, F., 2022. A novel $CuBi_2O_4$/polyaniline composite as an efficient photocatalyst for ammonia degradation. Heliyon 8 (8), e10210.
Akti, F., Balci, S., 2022. Synthesis of APTES and alcohol modified Sn/SBA-15 in presence of competitive ion: test in degradation of remazol yellow. Mater. Res. Bull. 145, 111496.
Akti, F., 2018. Photocatalytic degradation of remazol yellow using polyaniline–doped tin oxide hybrid photocatalysts with diatomite support. Appl. Surf. Sci. 455, 931–939.
Al-Tohamy, R., Ali, S.S., Li, F., Okasha, K.M., Mahmoud, Y.A.G., Elsamahy, T., Sun, J., 2022. A critical review on the treatment of dye-containing wastewater: ecotoxicological and health concerns of textile dyes and possible remediation approaches for environmental safety. Ecotoxicol. Environ. Saf. 231, 113160.
Ayub, A., Raza, Z.A., Majeed, M.I., Tariq, M.R., Irfan, A., 2020. Development of sustainable magnetic chitosan biosorbent beads for kinetic remediation of arsenic contaminated water. Int. J. Biol. Macromol. 163, 603–617.
Bag, S.S., Sinha, S., Banerjee, A., Golder, A., 2022. Simultaneous sensing and photocatalytic degradation to free water from toxic dye pollutants for possible agricultural and household applications: role of generated holes and hydroxyl radicals. J. Environ. Chem. Eng. 10 (6), 108919.
Bano, D., Chandra, S., Yadav, P.K., Singh, V.K., Hasan, S.H., 2020. Off-on detection of glutathione based on the nitrogen, sulfur codoped carbon quantum dots@ MnO_2 nano–composite in human lung cancer cells and blood serum. J. Photochem. Photobiol. A 398, 112558.
Benchikh, I., Dahou, F.Z., Lahreche, S., Sabantina, L., Benmimoun, Y., Benyoucef, A., 2022. Development and characterisation of novel hybrid materials of modified ZnO-SiO_2 and polyaniline for adsorption of organic dyes. Int. J. Environ. Anal. Chem. 102, 1–20.
Bhat, A.P., Gogate, P.R., 2021. Degradation of nitrogen-containing hazardous compounds using advanced oxidation processes: a review on aliphatic and aromatic amines, dyes, and pesticides. J. Hazard. Mater. 403, 123657.
Bhatt, P., Gangola, S., Bhandari, G., Zhang, W., Maithani, D., Mishra, S., Chen, S., 2021. New insights into the degradation of synthetic pollutants in contaminated environments. Chemosphere 268, 128827.
Bolisetty, S., Peydayesh, M., Mezzenga, R., 2019. Sustainable technologies for water purification from heavy metals: review and analysis. Chem. Soc. Rev. 48 (2), 463–487.
Chen, J., Xiong, Y., Duan, M., Li, X., Li, J., Fang, S., Zhang, R., 2019. Insight into the synergistic effect of adsorption–photocatalysis for the removal of organic dye pollutants by Cr-doped ZnO. Langmuir 36 (2), 520–533.
Chen, Z., Sun, S., Prakash, J., 2022. Design and engineering of graphene nanostructures as independent solar-driven photocatalysts for emerging applications in the field of energy and environment. Mol. Syst. Des. Eng. 7 (3), 213–238.
Dashairya, L., Sharma, M., Basu, S., Saha, P., 2019. SnS_2/RGO based nanocomposite for efficient photocatalytic degradation of toxic industrial dyes under visible-light irradiation. J. Alloys Compd. 774, 625–636.
Doh, S.J., Kim, C., Lee, S.G., Lee, S.J., Kim, H., 2008. Development of photocatalytic TiO_2 nanofibers by electrospinning and its application to degradation of dye pollutants. J. Hazard. Mater. 154 (1–3), 118–127.
Gadore, V., Mishra, S.R., Ahmaruzzaman, M., 2023. Green and environmentally sustainable fabrication of SnS_2 quantum dots/chitosan nanocomposite for enhanced photocatalytic performance: effect of process variables, and water matrices. J. Hazard. Mater. 444, 130301.
Ghanbari, F., Moradi, M., 2017. Application of peroxymonosulfate and its activation methods for degradation of environmental organic pollutants. Chem. Eng. J. 310, 41–62.
Guo, M., Yuan, B., Sui, Y., Xiao, Y., Dong, J., Yang, L., Chen, H., 2023. Rational design of molybdenum sulfide/tungsten oxide solar absorber with enhanced photocatalytic degradation toward dye wastewater purification. J. Colloid Interface Sci. 631, 33–43.
He, X., He, T., Liu, Y., Zhou, Y., Song, B., Qi, Y., Kang, Z., 2022. Enhanced adsorption and near-infrared photo reduction of Cr (VI) on polyaniline modified SnS2 nanosheets. Appl. Surf. Sci. 606, 154936.
Iqbal, A., Ahmed, A.S., Ahmad, N., Shafi, A., Ahamad, T., Khan, M.Z., Srivastava, S., 2021. Biogenic synthesis of CeO_2 nanoparticles and its potential application as an efficient photocatalyst for the degradation of toxic amido black dye. Environ. Nanotechnol. Monit. Manag. 16, 100505.
Jenifer, A., Sriram, S., 2023. Enhanced photocatalytic organic dye degradation activities of pristine and Zn-doped V_2O_5 nanoparticles. Appl. Surf. Sci. 611, 155629.
Khan, M.D.A., Akhtar, A., Nabi, S.A., Khan, M.A., 2014. Synthesis, characterization, and photocatalytic activity of polyaniline-Sn (IV) iodophosphate nanocomposite: its application in wastewater detoxification. Ind. Eng. Chem. Res. 53 (39), 15253–15260.
Khan, Y., Ahmad, A., Ahmad, N., Mir, F.R., Schories, G., 2020. Biogenic synthesis of a green tea stabilized PPy/SWCNT/CdS nanocomposite and its substantial applications, photocatalytic degradation and rheological behavior. Nanoscale Adv. 2 (4), 1634–1645.
Khan, T., Rahman, Q.I., Raza, S., Zehra, S., Ahmad, N., Husen, A., 2023. Nanodimensional materials: an approach toward the biogenic synthesis. In: Advances in Smart Nanomaterials and Their Applications. Elsevier, pp. 523–568.
Lei, Y., Song, S., Fan, W., Xing, Y., Zhang, H., 2009. Facile synthesis and assemblies of flowerlike SnS_2 and In^{3+}-doped SnS_2: hierarchical structures and their enhanced photocatalytic property. J. Phys. Chem. C 113 (4), 1280–1285.
Lellis, B., Fávaro-Polonio, C.Z., Pamphile, J.A., Polonio, J.C., 2019. Effects of textile dyes on health and the environment and bioremediation potential of living organisms. Biotechnol. Res. Innov. 3 (2), 275–290.
Lin, C., Zhu, M., Zhang, T., Liu, Y., Lv, Y., Li, X., Liu, M., 2017. Cellulose/SnS_2 composite with enhanced visible-light photocatalytic activity prepared by microwave-assisted ionic liquid method. RSC Adv. 7 (20), 12255–12264.
Mahanta, D., Manna, U., Madras, G., Patil, S., 2011. Multilayer self-assembly of TiO_2 nanoparticles and polyaniline-grafted-chitosan copolymer (CPANI) for photocatalysis. ACS Appl. Mater. Interfaces 3 (1), 84–92.
Matyszczak, G., Jóźwik, P., Polesiak, E., Sobieska, M., Krawczyk, K., Jastrzębski, C., Płociński, T., 2021. Sonochemical preparation of SnS and SnS_2 nano-and micropowders and their characterization. Ultrason. Sonochem. 75, 105594.
Muslim, M., Ali, A., Kamaal, S., Ahmad, M., Alam, M.J., Rahman, Q.I., Shahid, M., 2022. Efficient adsorption and facile photocatalytic degradation of organic dyes over H-bonded proton-transfer complex: an experimental and theoretical approach. J. Mol. Liq. 347, 117951.

Nawaz, S., Khan, Y., Abdelmohsen, S.A., Khalid, S., Björk, E.M., Rasheed, M.A., Siddiq, M., 2022. Polyaniline inside the pores of high surface area mesoporous silicon as composite electrode material for supercapacitors. RSC Adv. 12 (27), 17228–17236.

Nepomuceno, N.C., Seixas, A.A.A., Medeiros, E.S., Mélo, T.J.A., 2021. Evaluation of conductivity of nanostructured polyaniline/cellulose nanocrystals (PANI/CNC) obtained via in situ polymerization. J. Solid State Chem. 302, 122372.

Parveen, N., Ansari, M.O., Cho, M.H., 2016. Route to high surface area, mesoporosity of polyaniline–titanium dioxide nanocomposites via one pot synthesis for energy storage applications. Ind. Eng. Chem. Res. 55 (1), 116–124.

Rahman, Q.I., Ali, A., Ahmad, N., Lohani, M.B., Mehta, S.K., Muddassir, M., 2020a. Synthesis and characterization of CuO rods for enhanced visible light driven dye degradation. J. Nanosci. Nanotechnol. 20 (12), 7716–7723.

Rahman, Q.I., Hasan, S., Ali, A., Mehta, S.K., Raja, M.A., Ahmad, N., Muddassir, M., 2020b. Synthesis and characterizations of nitrogen (N) doped strontium titanate ($SrTiO_3$) nanoparticles for enhanced visible light driven photocatalytic degradation. J. Nanosci. Nanotechnol. 20 (10), 6475–6481.

Saadati, A., Sheibani, S., 2022. Insight into the adsorption and photocatalytic properties of in-situ synthesized g-C_3N_4/SnS_2 nanocomposite. Ceram. Int. 48 (20), 30294–30306.

Sagadevan, S., Alshahateet, S.F., Lett, J.A., Fatimah, I., Sivasankaran, R.P., Sibhatu, A.K., Soga, T., 2022. Highly efficient photocatalytic degradation of methylene blue dye over Ag_2O nanoparticles under solar light irradiation. Inorg. Chem. Commun. 148, 110288.

Sayed, M.A., Ahmed, M.A., El-Shahat, M.F., El-Sewify, I.M., 2022. Mesoporous polyaniline/SnO_2 nanospheres for enhanced photocatalytic degradation of bio-staining fluorescent dye from an aqueous environment. Inorg. Chem. Commun. 139, 109326.

Senasu, T., Hemavibool, K., Nanan, S., 2018. Hydrothermally grown CdS nanoparticles for photodegradation of anionic azo dyes under UV-visible light irradiation. RSC Adv. 8 (40), 22592–22605.

Serrano-Martínez, A., Mercader-Ros, M.T., Martínez-Alcalá, I., Lucas-Abellán, C., Gabaldón, J.A., Gómez-López, V.M., 2020. Degradation and toxicity evaluation of azo dye direct red 83: 1 by an advanced oxidation process driven by pulsed light. J. Water Process Eng. 37, 101530.

Sultana, S., Ahmad, N., Faisal, S.M., Owais, M., Sabir, S., 2017. Synthesis, characterisation and potential applications of polyaniline/chitosan-Ag-nano-biocomposite. IET Nanobiotechnol. 11 (7), 835–842.

Sultana, S., Ahmad, N., Ahmad, E., Sabir, S., Khan, M.Z., 2020. Electrochemical synthesis of novel aluminium oxyhydroxide-decorated MnO_2/chitosan nanocomposite with efficient photocatalytic and antibacterial activity. Nanotechnol. Environ. Eng. 5, 1–12.

Toumi, I., Djelad, H., Chouli, F., Benyoucef, A., 2022. Synthesis of PANI@ ZnO hybrid material and evaluations in adsorption of congo red and methylene blue dyes: structural characterization and adsorption performance. J. Inorg. Organomet. Polym. Mater. 32 (1), 112–121.

Varjani, S., Rakholiya, P., Ng, H.Y., You, S., Teixeira, J.A., 2020. Microbial degradation of dyes: an overview. Bioresour. Technol. 314, 123728.

Wu, W., Jiang, C., Roy, V.A., 2015a. Recent progress in magnetic iron oxide–semiconductor composite nanomaterials as promising photocatalysts. Nanoscale 7 (1), 38–58.

Wu, Z., Xue, Y., Zhang, Y., Li, J., Chen, T., 2015b. SnS_2 nanosheet-based microstructures with high adsorption capabilities and visible light photocatalytic activities. RSC Adv. 5 (31), 24640–24648.

Xiong, P., Wang, L., Sun, X., Xu, B., Wang, X., 2013. Ternary titania–cobalt ferrite–polyaniline nanocomposite: a magnetically recyclable hybrid for adsorption and photodegradation of dyes under visible light. Ind. Eng. Chem. Res. 52 (30), 10105–10113.

Xu, Z., Zhang, Z., Gao, L., Lin, H., Xue, L., Zhou, Z., Zhuo, S., 2018. Tin disulphide/nitrogen-doped reduced graphene oxide/polyaniline ternary nanocomposites with ultra-high capacitance properties for high rate performance supercapacitor. RSC Adv. 8 (70), 40252–40260.

Yang, F., Han, G., Fu, D., Chang, Y., Wang, H., 2013. Improved photodegradation activity of TiO_2 via decoration with SnS_2 nanoparticles. Mater. Chem. Phys. 140 (1), 398–404.

Yontar, A.K., Avcioğlu, S., Çevik, S., 2022. Nature-based nanocomposites for adsorption and visible light photocatalytic degradation of methylene blue dye. J. Clean. Prod. 380, 135070.

Zai, J., Wei, X., Sun, M., Tian, H., Liu, X., Qi, R., Qian, X., 2021. Light absorption, photocarrier dynamic properties of hierarchical SnS2 microspheres and their performances on photodegradation of high concentration Rhodamine B. J. Photochem. Photobiol. A 415, 113320.

Zhang, Z., Shao, C., Li, X., Sun, Y., Zhang, M., Mu, J., Liu, Y., 2013. Hierarchical assembly of ultrathin hexagonal SnS_2 nanosheets onto electrospun TiO_2 nanofibers: enhanced photocatalytic activity based on photoinduced interfacial charge transfer. Nanoscale 5 (2), 606–618.

Zhang, Y.C., Yao, L., Zhang, G., Dionysiou, D.D., Li, J., Du, X., 2014. One-step hydrothermal synthesis of high-performance visible-light-driven SnS_2/SnO_2 nanoheterojunction photocatalyst for the reduction of aqueous Cr (VI). Appl. Catal. B 144, 730–738.

Zhang, Y., Hu, L., Zhou, H., Wang, H., Zhang, Y., 2022. NIR photothermal-enhanced electrocatalytic and photoelectrocatalytic hydrogen evolution by polyaniline/SnS_2 nanocomposites. ACS Appl. Nano Mater. 5 (1), 391–400.